ACS NANO
Cite This: ACS Nano 2018, 12, 4719−4726
www.acsnano.org

ARTICLE

Double Indirect Interlayer Exciton in a $MoSe_2$/WSe_2 van der Waals Heterostructure

Aubrey T. Hanbicki,*,† Hsun-Jen Chuang,†,‡ Matthew R. Rosenberger,§ C. Stephen Hellberg, Saujan V. Sivaram,§ Kathleen M. McCreary, Igor I. Mazin, and Berend T. Jonker

Materials Science & Technology Division, Naval Research Laboratory, Washington, D.C. 20375, United States

Supporting Information

ABSTRACT: An emerging class of semiconductor heterostructures involves stacking discrete monolayers such as transition metal dichalcogenides (TMDs) to form van der Waals heterostructures. In these structures, it is possible to create interlayer excitons (ILEs), spatially indirect, bound electron−hole pairs with the electron in one TMD layer and the hole in an adjacent layer. We are able to clearly resolve two distinct emission peaks separated by 24 meV from an ILE in a $MoSe_2$/WSe_2 heterostructure fabricated using state-of-the-art preparation techniques. These peaks have nearly equal intensity, indicating they are of common character, and have *opposite* circular polarizations when excited with circularly polarized light. *Ab initio* calculations successfully account for these observations: they show that both emission features originate from excitonic transitions that are indirect in momentum space and are split by spin−orbit coupling. Also, the electron is strongly hybridized between both the $MoSe_2$ and WSe_2 layers, with significant weight in both layers, contrary to the commonly assumed model. Thus, the transitions are not purely interlayer in character. This work represents a significant advance in our understanding of the static and dynamic properties of TMD heterostructures.

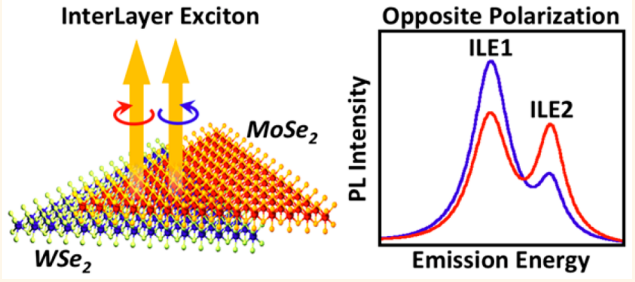

KEYWORDS: *transition metal dichalcogenides, 2D heterostructure, $MoSe_2$, WSe_2, two-dimensional materials, valley polarization, photoluminescence, density functional theory*

Tailoring semiconductor heterostructures for specific functionalities has led to varied optoelectronic devices including solar cells, photodetectors, light-emitting diodes, and lasers. An emerging class of heterostructures involves stacking discrete monolayers such as the transition metal dichalcogenides (TMDs)[1,2] to form so-called van der Waals heterostructures (vdWHs).[3,4] vdWHs offer myriad functionalities, making them promising hosts for future devices. One intriguing new property is the formation of an interlayer exciton (ILE), a spatially indirect, bound electron−hole pair with the electron in one TMD layer and the hole in an adjacent layer.[5−14]

$MoSe_2$/WSe_2 is a bilayer vdWH composed of isoelectronic Mo and W diselenide monolayers. It has a type II band alignment with a *spatially indirect* minimal excitation gap, with the top of the valence band formed predominantly by W states and the bottom of the conduction band by Mo states.[15−18] ILE emission in this heterostructure has recently been observed,[8−13] indicating significant dipole transitions between layers. The reported photoluminescence (PL) energy of the ILE emission is in the range of 1.35−1.4 eV. Due to the type II band alignment of the heterostructure,[15−18] this energy is well separated from the room-temperature emission energies of the constituent $MoSe_2$ (1.55 eV)[19] and WSe_2 (1.65 eV)[20] monolayers. As in the isolated monolayers, the heterostructure violates inversion symmetry, resulting in spin−orbit splitting of the bands. While interlayer excitons have been reported in systems such as WSe_2/MoS_2,[5] MoS_2/WS_2,[6,7] and $MoSe_2$/MoS_2,[14] we confine our discussion and comparison to the $MoSe_2$/WSe_2[8−13] system because the lattice matching and ordering of the conduction band splitting in other systems could produce fundamentally different results.

Two groups have reported a splitting of the ILE in $MoSe_2$/WSe_2 at low temperature. Both groups use samples consisting of bare $MoSe_2$/WSe_2 heterostructures, and the splitting was not well resolved.[8,13] The origin of this splitting and indeed of the ILE itself has not been clarified. One group reports the splitting to be on the order of 25 meV and suggests the two peaks originate from the bright and dark excitons at the K-point, with both transitions direct in momentum space.[8] The 25 meV splitting in emission energy agrees well with the calculated *ab initio* spin−orbit (SO) splitting of the $MoSe_2$ conduction band at the K-point.[21] Another group deconvolves their data into two

Received: February 20, 2018
Accepted: May 4, 2018
Published: May 4, 2018

DOI: 10.1021/acsnano.8b01369
ACS Nano 2018, 12, 4719−4726

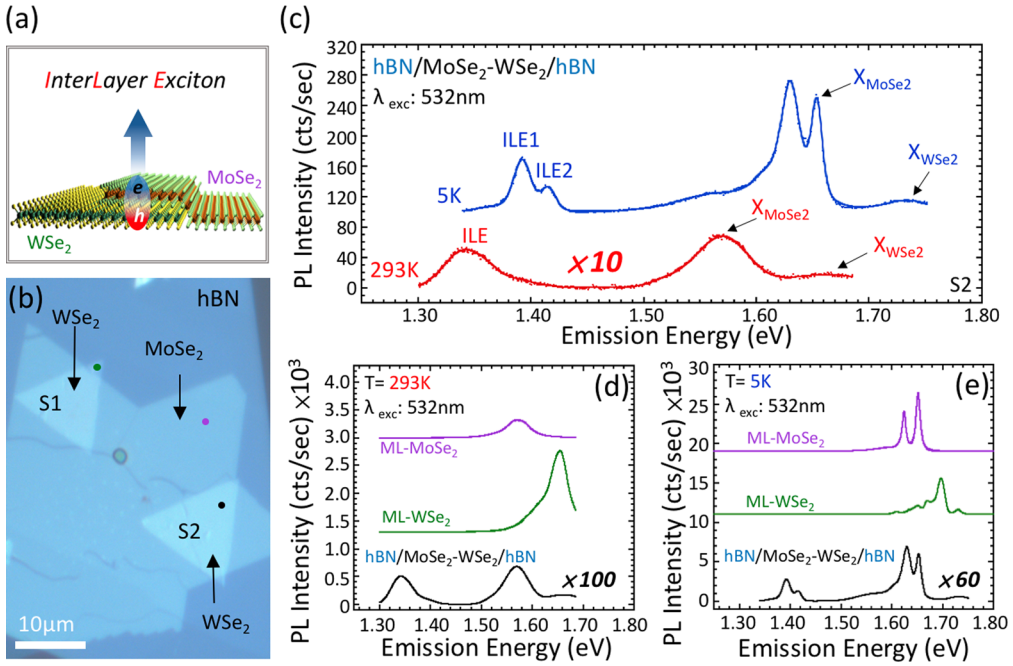

Figure 1. Characterization of the interlayer exciton. (a) Schematic depiction of the $MoSe_2/WSe_2$ heterostructure. (b) Optical micrograph of two vdWH samples, S1 and S2, before capping with the top hBN layer for ease of visualization. The brighter triangles are the CVD ML-WSe_2, and the larger star-like shaped layer is the CVD ML-$MoSe_2$. The colored dots indicate the position where PL data were acquired. (c) PL of the interlayer exciton from sample S2 at room temperature (red) and 5 K (blue). A comparison of the PL from the interlayer exciton, monolayer $MoSe_2$, and monolayer WSe_2 regions is shown at (d) 293 K and (e) 5 K. Spectra in (c)−(e) are offset for clarity, and scaling factors are indicated as necessary. The ground state exciton emission features from the individual $MoSe_2$ and WSe_2 layers are labeled X_{MoSe2} and X_{WSe2}, respectively.

peaks separated by almost 40 meV.[13] They propose one of the peaks corresponds to a transition indirect in real space yet direct in momentum space, while the second feature is indirect in both real and momentum space. Both scenarios are inconsistent with the similar intensity observed for the two ILE peaks.

In this work, by using advanced preparation techniques, we fabricate a vdWH in which we are able to resolve the ILE splitting clearly, enabling us to elucidate the nature of the ILE and the origin of these features. The split emission features exhibit nearly equal intensity and opposite polarizations that vary in a nonmonotonic fashion with excitation energy. Based on considerations of their relative intensities, opposite polarizations, and *ab initio* calculations, we conclude that both transitions are indirect in momentum space, in contrast with previous interpretations. The valence band maxima (hole states) occur at the K, K′ points in the Brillouin zone, while the conduction band minima (electron states) occur at the Q, Q′ points. Both bands exhibit splittings due to SO effects. Furthermore, although the electron in the interlayer exciton is commonly thought to reside entirely in the Mo layer, we find instead that it has significant weight in both layers at Q. In contrast, the electron states reside entirely in the Mo layer at the K-point.

We find that including interlayer hybridization is essential to theoretically determine the ILE character. The hybridized electron eigenstates are superpositions of both spin states, and both spin−orbit split bands are optically bright, decaying optically with holes at the K point with opposite polarizations. The Q−K transition is suppressed in momentum space relative to the direct transition at K because it is indirect and requires either a phonon or defect scattering to conserve momentum. But since the relevant wave function at Q has comparable weight in both layers, it has significant overlap in real space. The lowest-energy direct transition at K is strongly suppressed because hybridization is forbidden by symmetry at this point (see Supporting Information). This scenario is qualitatively different from previous models and accounts for the roughly equivalent emission intensity of both peaks, and is consistent with the raw data previously reported for this heterostructure.[8,13] Our layer- and spin-resolved band structure calculations provide insight into the origin of the ILE, and suggest ways to tailor the indirect/direct momentum space character of one or both transitions.

RESULTS

$MoSe_2$ on WSe_2 Heterostructures. We prepared a number of $MoSe_2$ on WSe_2 heterostructures, and a schematic of the resulting system is shown in Figure 1a. Typical results are summarized here, and a more detailed account is presented in the Supporting Information (SI). The individual monolayer components were synthesized using chemical vapor deposition (CVD) and transferred with a transfer technique described in the Methods section and illustrated in Figure SI-1. Two samples discussed in the main text are shown in the optical micrograph of Figure 1b. In this image, there are two monolayer (ML) WSe_2 triangles on top of hexagonal boron nitride (hBN) with a larger ML $MoSe_2$ flake draped over them. The edges of both WSe_2 triangles in Figure 1b are aligned within <3° of the edges of the $MoSe_2$. Hereafter, we will refer to the $MoSe_2/WSe_2$ overlap regions as S1 and S2, as labeled in the figure. A third sample (S3) was also fabricated with a misalignment of ∼28°. In each case, the structure is capped with a second layer of hBN (not shown in Figure 1b for clarity).

DOI: 10.1021/acsnano.8b01369
ACS Nano 2018, 12, 4719−4726

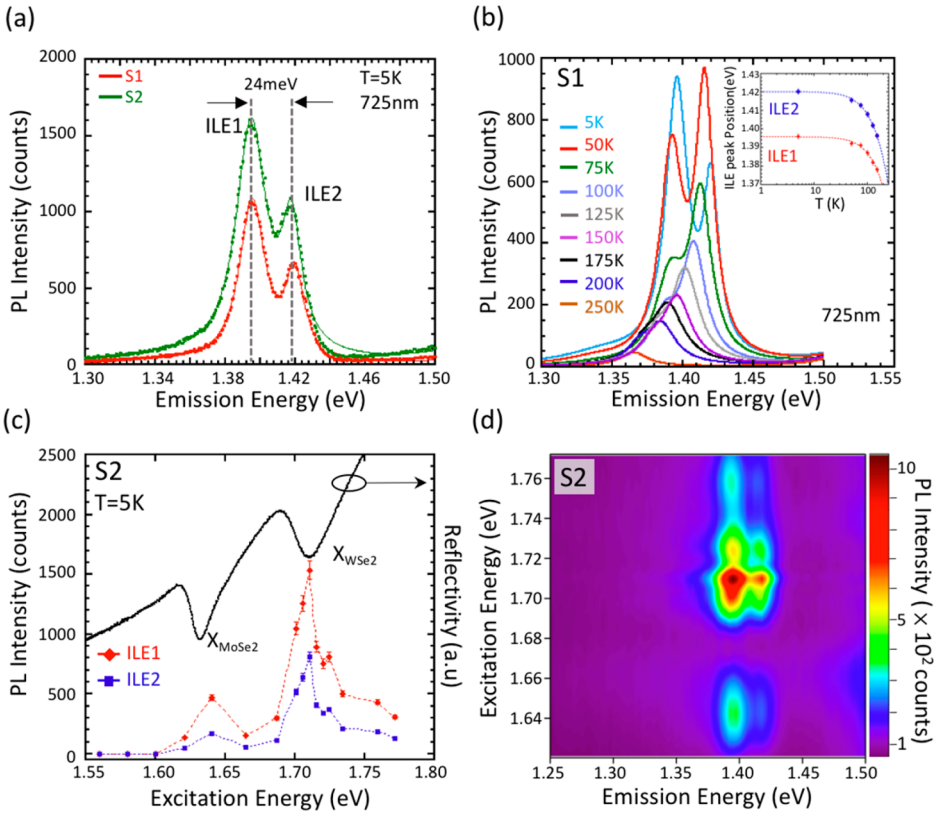

Figure 2. Emission from two ILEs: (a) Interlayer exciton PL at low temperature showing two well-resolved peaks, ILE1 and ILE2. An excitation energy of 1.710 eV (725 nm) was used, and spectra from both S1 (red) and S2 (green) are shown. (b) Temperature-dependent PL measurement of S1. The inset shows the peak shift for each emission line and follows a standard semiconductor behavior. (c) PL peak intensity of ILE1 (red points) and ILE2 (blue points) at different excitation energies from S2. The black line is the differential reflectivity measurement of S2. (d) PLE heat map of S2 showing splitting of the ILE and intensity maxima at resonant energies.

Atomic force microscopy (AFM) images from all of our samples are presented in Figures SI-2 and SI-3.

To reduce inhomogeneity and increase intimate contact between layers, we incorporated several advances in sample preparation. First, we have encapsulated the entire structure within hBN, which significantly reduces the inhomogeneous contributions to PL line widths by providing surface protection as well as substrate flatness.[22,23] Even in encapsulated samples, interlayer imperfections persist.[24] Therefore, we also flattened areas of the sample using an AFM as a squeegee,[25] as described in the Methods section and shown in Figures SI-2 and SI-3. We are thus able to remove a considerable amount of residual material between the two TMD monolayers in a select area of the overlap region, resulting in an intimate and reproducible contact. The advantage of the AFM squeegee procedure manifests itself in two ways. First, while the ILE intensity is higher in hBN-encapsulated samples, splitting of the ILE is only apparent in AFM flattened regions. Second, in room-temperature Raman spectra from the flattened region the B^1_{2g} feature emerges. This feature is expected from both bilayer $MoSe_2$ and WSe_2 and therefore is a strong indication of an interaction between the monolayers. These effects are detailed further in the Supporting Information.

A summary of the PL from various spots on our sample is shown in Figure 1c–e using an excitation energy of 2.33 eV (532 nm). The physical location where each spectrum was collected is indicated by dots on Figure 1b and color coded with the spectra. As expected, reference PL spectra from the individual $MoSe_2$ and WSe_2 layers exhibit strong peaks at 1.57 and 1.65 eV, respectively, at room temperature (Figure 1d) and 1.65 and 1.71 eV at 5 K (Figure 1e). In the encapsulated and AFM flattened overlap regions S1 and S2, the WSe_2 and $MoSe_2$ emission is strongly quenched, as can be clearly seen in these figures. This is expected and has been attributed to the ultrafast charge separation enabled by the close proximity of these monolayers.[26] Our PL and reflectivity lines are somewhat broader than those reported in single layers of encapsulated TMDs,[22,23] albeit much narrower than in unencapsulated heterostructures. Intrinsic broadening of line widths in heterostructures has been reported elsewhere and attributed to the fundamental optical processes in heterostructures.[27] Further broadening could be due to the relative quality of our samples as well as the lengthy procedure in ambient required to assemble the structure.[24] We also note that the dielectric environment of a heterostructure will be somewhat different than that of individual layers sandwiched between hBN. Further characterization of all our samples, including Raman spectroscopy, is presented in the SI Section SI-2 and corroborates the interacting nature and reproducibility of the $MoSe_2/WSe_2$ vdWHs.

An Interlayer Exciton Emerges. A new emission feature emerges at 1.35 eV at room temperature in the overlap regions (Figure 1c). This feature has commonly been associated with the ILE.[8−13] The intensity of the ILE PL is slightly different for both samples, and the spatial variation of the ILE peak intensity is mapped in Figure SI-2 for both S1 and S2. In the flattened region, the ILE emission has areas where it is uniform, although there is some inhomogeneity related to sample damage

DOI: 10.1021/acsnano.8b01369
ACS Nano 2018, 12, 4719−4726

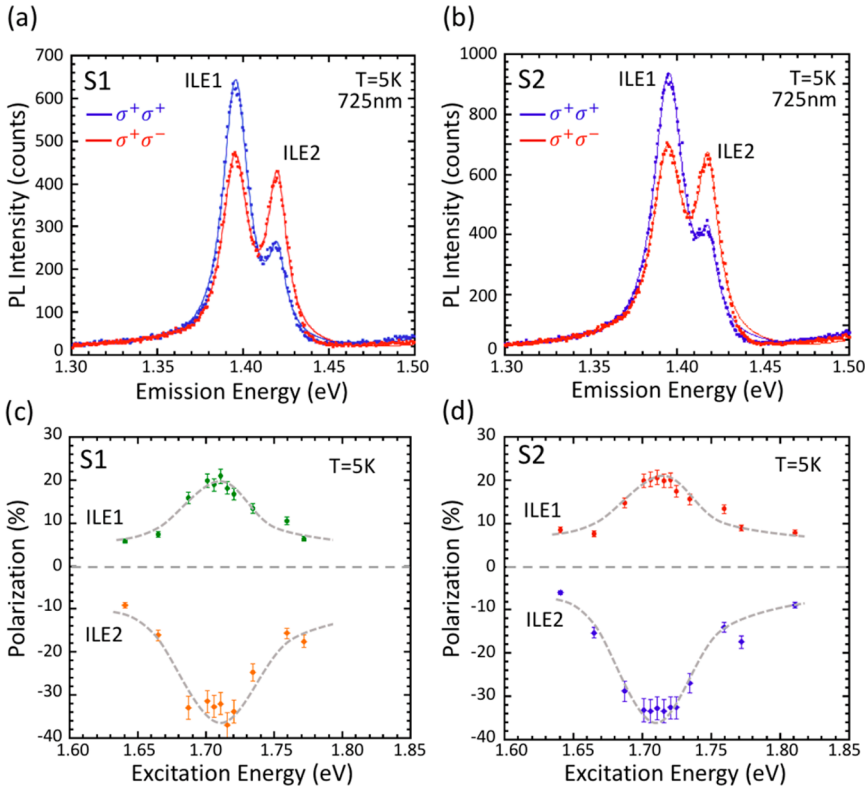

Figure 3. Opposite circular polarization from each ILE. PL measurements using a circularly polarized excitation at 1.710 eV (725 nm) and analyzing for the same (blue) and opposite (red) helicity for (a) S1 and (b) S2 at 5 K. A summary of the polarization of each peak as a function of excitation energy is shown for (c) S1 and (d) S2. The gray dashed line is a guide for the eye.

introduced during fabrication (Figure SI-2). The ILE is also observed for a sample that was flattened but not encapsulated, sample S0. It is not observed in S3, the intentionally misaligned heterostructure, consistent with recent reports.[11] Further characterizations of S0−S3 are presented in Section SI-2.

When the sample is cooled to 5 K, the ILE peak exhibits a well-resolved splitting with distinct peaks at 1.396 eV (ILE1) and 1.420 eV (ILE2), as shown in Figure 2a for samples S1 and S2. A similar plot for all of the samples is presented in Figure SI-8. The line widths of these peaks are 20 meV (ILE1) and 13 meV (ILE2), significantly narrower than the widths of 45 and 30 meV reported by Rivera *et al.*[8] The high resolution of our spectra enable us to accurately determine the splitting to be 24 ± 1 meV, similar to the splitting inferred by Rivera *et al.*[8] This splitting is seen over the entire flattened overlap area. The ILE splitting is unlikely to be caused by a charged exciton because we observe opposite circular polarizations in our two peaks, as discussed below. The creation of a trion could lower the overall polarization, but not produce a peak with opposite polarization.[28,29]

The temperature dependence of the ILE features is shown in Figure 2b. A full discussion of the temperature dependence and power dependence of these peaks is provided in Sections SI-4 and SI-5. In brief, the temperature dependence of the peak positions follows a standard semiconductor behavior, as shown by the inset in Figure 2b and in Figure SI-13, providing good evidence of intrinsic behavior from a uniform, intimate contact between our layers. The evolution of the relative strength of the two peaks with both increasing temperature and excitation power is presented in Figures SI-9 to SI-14.

The data in Figure 2a,b were taken with an excitation wavelength of 1.710 eV (725 nm). The reason for this choice is clear from Figure 2c,d. Figure 2c shows the PL peak intensity for ILE1 (red points) and ILE2 (blue points) at 5 K as a function of excitation energy. The differential reflectivity (Figure 2c, solid black line) shows a strong correlation of optical absorption with the maxima in the ILE PL intensity at 1.71 eV. A heat map of these data is shown in Figure 2d, confirming this correlation. We did not observe any signature of a charged exciton transition in differential reflectivity. This indicates a small oscillator strength and suggests both monolayers have a low level of doping.[30]

Circular Polarization. A very striking behavior is observed upon excitation with circularly polarized light. We find that ILE1 and ILE2 both exhibit significant polarization, as reported previously.[9,13] But contrary to these reports, we find the polarizations are of *opposite* sign and exhibit a nonmonotonic dependence upon excitation energy, as shown in Figure 3. Most single-layer TMDs are semiconductors with a direct gap[31] at the K-points and are well-known for their potential as valleytronic materials because they have two inequivalent, but related K-points in the Brillouin zone, K and K′.[32−34] By symmetry, the valence band maxima at K and K′ have opposite spin states, giving these materials distinct optical selection rules.[32−35] Using circularly polarized light, it is possible to selectively populate and interrogate the different valleys, K or K′, and valuable information on the nature of the bands can be derived from studies of polarization-resolved emission.

The spectra in Figure 3 were obtained with a circularly polarized excitation source of energy 1.710 eV (725 nm). The excitation has positive helicity ($\sigma+$), and we analyze the PL for positive and negative helicity ($\sigma-$). Polarization is defined as $P = [I(\sigma+) - I(\sigma-)]/[I(\sigma+) + I(\sigma-)]$, where $I(\sigma\pm)$ is the emission intensity analyzed for positive (negative) helicity. It is

DOI: 10.1021/acsnano.8b01369
ACS Nano 2018, 12, 4719−4726

clear from the raw spectra shown in Figure 3a,b for vdWH samples S1 and S2 that the ILE1 and ILE2 emission peaks have opposite circular polarizations. These spectra can be well fit with two Lorentzians, as illustrated in Figure SI-6, to quantitatively determine the polarization of each feature. The polarization of ILE1 and ILE2 as a function of excitation energy is shown in Figure 3c,d for vdWH samples S1 and S2, respectively. Significantly, the peaks have opposite polarizations for all excitation energies, and the magnitude of the polarization for each feature exhibits a pronounced nonmonotonic behavior with a strong peak at 1.71 eV, corresponding to the absorption feature in the WSe_2 (Figure 2c). This behavior persists to 120 K, as shown in Figure SI-11. Prior studies on the $MoSe_2/WSe_2$ heterostructure have shown only a positive polarization for the ILE;[9,13] because separate peaks were never clearly resolved, the behavior shown in Figure 3 was not visible. Polarizations of opposite sign were noted in a system where monolayer WSe_2 was subjected to a large magnetic field,[36] but the reason or mechanism for the opposite handedness was not determined. The fact that the magnitude of polarization is nearly twice as large for ILE2 suggests that the opposite signs are not symmetry-defined but have a quantitative nature.

DISCUSSION

In order to understand this polarization behavior and the detailed nature of the ILE excitons, we have computed the band structure of the $MoSe_2/WSe_2$ vdWH using density functional theory (DFT). The results are shown in Figure 4a, where the color coding indicates the layer from which the states are derived and the arrows indicate the spin orientation. Details of the calculations are given in the Methods section. The valence band maximum (VBM) lies at K and K′ and is localized entirely within the WSe_2 layer; the corresponding W-derived states have quantum numbers $L_z = 2$, $S_z = 1/2$, so the spin at the VBM, indicated by arrows in Figure 4a, is parallel to z, the direction perpendicular to the layers. The lowest conduction band at K is a pure Mo-derived state, with $L_z = -1$, $S_z = 1/2$. However, the minimal gap is indirect and occurs at a point labeled Q between Γ and K. Isoenergetic surfaces (Figure 4b) indicate that the absolute conduction band minimum (CBM) is located at the Q-point.

The electron density of the conduction and valence bands at the band edges is shown in Figure 4c. From this figure it is clear the CBM at Q is strongly hybridized, with significant contributions from both the $MoSe_2$ and WSe_2 layers: note the common isosurfaces on both the Mo and W atoms. In contrast, both the conduction band and valence band edge states at K exhibit negligible hybridization. There are two reasons for this: first, the point symmetry at the K-point suppresses hybridization, while Q has a lower symmetry; second, the bare W and Mo bands come closer to each other at Q than at K. Previous work has shown that the band edge states at K have negligible hybridization in DFT.[37]

Optical transitions involving recombining electrons and holes residing predominantly on different lattice sites are only possible because of the overlap of the corresponding orbitals. In a vdWH structure, by definition, this overlap is very small (otherwise the bonding would be covalent). As discussed, since the hybridization between the two layers at the K-point is suppressed by symmetry, the states at K are either pure W or pure Mo in character. The dipole matrix elements between unlike states, even when spin-allowed, are strongly suppressed (although not entirely forbidden) by the small interlayer orbital

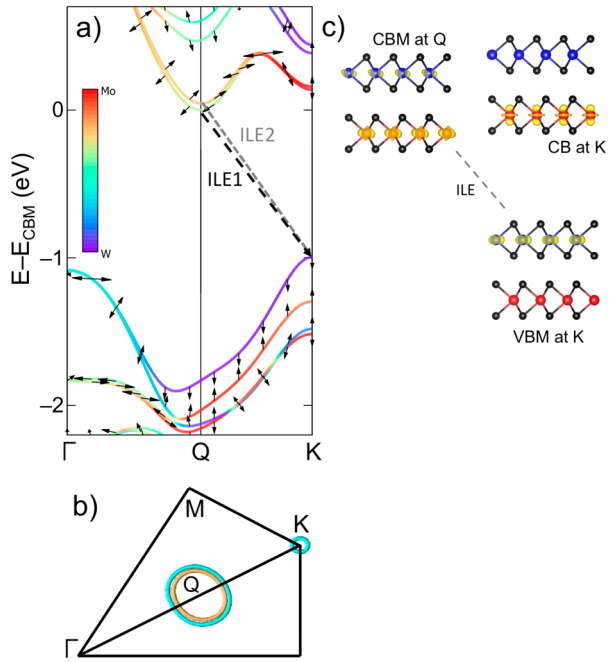

Figure 4. Results of density functional calculations. (a) Band structure of the $MoSe_2/WSe_2$ heterostructure. The conduction band minimum lies at the Q-point. The color indicates the layer from which the states are derived: red is pure $MoSe_2$; purple is pure WSe_2. The spin direction (integrated over the entire cell) is in the $y-z$ plane (x is defined by Γ−K). The two lowest energy transitions, ILE1 and ILE2, are indicated with dashed lines. The SO splitting of the valence band is large, while that in the conduction band is much smaller. (b) Isoenergetic surfaces in the conduction band for the irreducible wedge of the Brillouin zone. The lowest two states occur at the Q-point (SO split), while the third lowest state appears at K. (c) Graphical representation of the electron density isosurfaces at the three points of the band structure indicated. The Mo are red, W are blue, Se are black, and the electron density isosurfaces are yellow. Higher resolution figures are shown in the Supporting Information.

overlap. As shown in Section SI-6, numerical calculations of the direct optical transition find that both SO-split transitions have a vanishing optical weight in the vicinity of K and cannot be associated with either of our observed excitons, contrary to some earlier proposals.[8,13]

At the Q-point, however, hybridization is allowed; it is small because the physical overlap is small, but since the bare W and bare Mo bands at the Q-point coincidentally lie close to each other, even a small hybridization amplitude causes sizable mixing. The CBM, therefore, has a considerable contribution from the WSe_2 layer (Figure 4a), and an optical transition from the Q-point to the K-point will always proceed on just the W site; that is, the electron and hole are in the same layer. In this sense, the transition is not purely interlayer in character and the dipole matrix elements for this transition are not suppressed by the small interlayer overlap. Furthermore, the hybridization between layers mixes bands with opposite spins, resulting in the tilting of the spins in regions of the CB away from the K-point. While mixing at Q is evidence of interlayer overlap at this point in the Brillouin zone, one can prove that intralayer localization at K is dictated by symmetry and does not indicate a total absence of overlap. This is addressed in the Supporting Information, Section SI-6.

DOI: 10.1021/acsnano.8b01369
ACS Nano 2018, 12, 4719−4726

As stated earlier, the CBM at the Q-point has considerable weight on W; the challenge is to calculate the dipole matrix elements for circularly polarized photons inside the W atomic sphere because the polarization is not dictated by crystal symmetry as it is for the direct, K−K transition. On the basis of the wave function character in density functional calculations (see Supporting Information, Section SI-6) we determine that the two indirect Q−K transitions are both allowed and have similar weight. Note that, while the heterostructure Q−K transition is bright compared to the direct K−K transition, it is of course not comparable to an intralayer (single-layer) direct exciton (see Figure 1d,e). Numerically, we then calculate the recombination between the CBM at Q and VBM at K and find the emission is predominantly positive helicity light, as observed for ILE1, while recombination between the higher SO split CB state at Q and the VBM at K emits mostly negative helicity photons, as observed for ILE2. Thus, we conclude that (1) the observed ILE occurs between the upper valence state at K and the two lowest, SO-split conduction states at Q and (2) the character of the states at Q is such that the ILE splits into predominantly positive and predominantly negative helicity peaks, a feature that should be investigated for potential applications. In our calculation, the SO splitting of the VBM at K is large, while that in the conduction band at Q is much smaller, which accounts for the relatively narrow observed splitting. Exciton binding, not included in our computations, will renormalize the optical matrix elements but will not significantly change their relative weights, as shown explicitly elsewhere.[37] Therefore, our *ab initio* calculations successfully account for the magnitude of the splitting, the similarity in intensity, and the opposite polarizations observed in the ILE peaks.

We have not considered moiré effects in our calculations, although twist angles could have an impact on the behavior of the ILE and should be explored. In the case of small angle mismatches, hybridization between the layers and thus the energy of the interlayer excitons (of any origin) will vary from point to point, and lateral momentum conservation will be fully relaxed. As a result, multiple peaks of reduced intensity are expected in moiré regions.[38,39] Reference 39 predicts such peaks and describes a dispersion in energy with the twist angle of ILE features derived from direct K−valley transitions. The predicted energy shift for a rotation angle of ∼1° is a significant fraction of the line width. We have not explored this systematically, but note that although samples S1 and S2 certainly exhibit small but different misalignments, we observe identical ILE peak energies and very similar overall behavior. This may be due to the indirect character of the transitions (Q to K), to the strong conduction band hybridization discussed earlier, or to experimental factors we have not adequately controlled. Thus, we conclude that our observed signal originates from the coherent (not moiré) parts of the sample.

In summary, we have fabricated high-quality $MoSe_2/WSe_2$ heterostructures and observe a well-resolved splitting of the interlayer exciton photoluminescence arising from the SO splitting of the conduction band. The two split features exhibit significant (20−35%) and opposite circular polarizations when excited with circularly polarized light, with maximum polarization occurring when excited resonantly at the WSe_2 absorption peak. By analyzing the individual properties of the two peaks, comparing with first-principles theory, and using general symmetry considerations, we are able to exclude the proposal that one or both of the two excitons are due to direct transitions at the K points. Instead, we find the two interlayer excitons are fully indirect in momentum space and partially indirect in real space. Contrary to the accepted model, the electrons in the ILEs have significant weight in both layers due to interlayer hybridization. The hybridization of the electrons between the layers tilts the electrons' spins, and both ILEs are optically bright with opposite polarizations. Our results have important implications on the utility of these systems for future electronic and valleytronic applications.

METHODS

Sample Preparation. *CVD Growth.* Monolayer $MoSe_2$ and WSe_2 are synthesized *via* atmospheric pressure CVD using solid precursors in a 2 in. quartz tube furnace. Silicon wafers with 275 nm thermally grown oxide (Silicon Valley Microelectronics, Inc.) and single-side polished *c*-plane sapphire (University Wafer) are used as the target substrates for $MoSe_2$ and WSe_2, respectively. Prior to growth, the substrates are cleaned by ultrasonication, piranha etching, and oxygen plasma exposure. Both TMD syntheses use a water-soluble seeding promoter, perylene-3,4,9,10-tetracarboxylic acid tetrapotassium salt (PTAS), that is drop-cast onto a clean SiO_2 substrate immediately before growth. A clean SiO_2 substrate or sapphire substrate is downstream from the PTAS substrate for $MoSe_2$ or WSe_2, respectively. The substrates are loaded face down on a quartz boat directly above the solid precursor (50 mg of MoO_2 (Sigma-Aldrich, 99%) or 1000 mg of WO_3 (Alfa Aesar, 99.998%)). The precursor and substrates are then moved to the center of the tube furnace. An additional quartz boat containing Se (Alfa Aesar, 99.999%) is placed upstream near the edge of the furnace. The tube is repeatedly evacuated to ∼100 mTorr and filled with UHP Ar and H_2. For $MoSe_2$, monolayer synthesis occurs at 750 °C, whereas WSe_2 requires a higher temperature of 950 °C.

Sample Transfer. The hBN-encapsulated heterostructure is prepared *via* a water-assisted pick up, dry transfer method and is fully detailed in the Supporting Information, Section SI-1, which includes a schematic of the transfer process. The full structure from top to bottom is 5 nm hBN/ML-$MoSe_2$/ML-WSe_2/20 nm-hBN/275 nm SiO_2/Si substrate for S1 and S2. In brief, the stack was picked up in reverse order with freshly prepared PDMS then transferred to the substrate.

PDMS Preparation. Polydimethylsiloxane (PDMS) is made from a commercially available SYLGARD 184 silicone elastomer kit. To make the PDMS mixture, we mix the two components thoroughly (Silicone Elastomer and curing agent) with a weight ratio of 10:1 followed by a debubbling process under rough vacuum. This mixture is spin coated on a silicon wafer with a spin rate of 350 rpm for 30 s, then cured at 80 °C for 30 min on a hot plate. The resultant PDMS is easily peeled off the silicon wafer for use.

AFM Flattening. This technique[25] more thoroughly removes residual material from between layers than the commonly used technique of annealing[11,40] and has a significantly smaller thermal budget since no heating is required. AFM flattening was performed on a Park Systems NX-10 AFM. The AFM cantilever used for flattening was an NCHR (Nanosensors) with a nominal spring constant of 42 N/m. The scan size for AFM flattening varied from 6 to 15 μm, depending on the desired size of the flattened region. The scan rate was typically 1 Hz, corresponding to a scan speed as high as 30 μm/s. The scan line density was typically 10 nm/line or less in order to maintain sufficient overlap between lines, which caused contaminants to be squeezed out of the flattened area rather than accumulating between scan lines. The required normal force to achieve good flattening depended on sample/tip-specific parameters, including the tip radius and hBN thickness. Generally, thicker hBN required larger normal force. To determine the appropriate normal force, the tip was first engaged with the minimum possible force, and then the force was increased while observing the topography. The force was increased until bubbles and wrinkles disappeared from the topography.

DOI: 10.1021/acsnano.8b01369
ACS Nano 2018, 12, 4719−4726

Sample Characterization. Temperature-dependent PL, Raman, and differential reflectivity spectra are acquired under vacuum conditions (pressure ~1 × 10^{-5} Torr) in a Janis ST-500 microscopy cryostat using a commercial Horiba LabRam HR Evolution confocal spectrometer. Beam steering mirrors control the laser position in the $x-y$ sample plane and enable both single spot and scanned area acquisition. Excitation sources include a tunable continuous-wave (CW) Ti:sapphire laser (Spectra-Physics) as well as various single-wavelength CW lasers for PL and Raman and a white light source (Energetiq−LDLS) for differential reflectivity. To enable comparison between the various lasers, we have used only CW sources.[41] A 50× objective (NA = 0.35) is used to focus the laser to a spot of ~2 μm diameter. A quarter-wave plate (Thorlabs superachromatic) is used to circularly polarize the laser excitations. The resulting photoluminescence is collected and directed through the same quarter-wave plate and a subsequent rotatable linear polarizer to analyze the circularly polarized emission components. We obtain the same polarization when the sample is excited with negative helicity light, and the emitted circular polarization is 0% when the sample is excited with linearly polarized light.

Theory. Most of the calculations presented here were performed using the generalized-gradient approximation[42] with the DFT-D3(BJ) van der Waals correction[43,44] and projector augmented wave functions as implemented in the Vienna *ab initio* simulation package (VASP).[45−47] A plane wave cutoff of 450 eV and a 4 × 4 Γ-centered k-point mesh were used. Atomic positions were relaxed until residual forces were less than 0.5 meV/Å. The lattice parameter was set to be the same for both layers, and the optimal lattice constant of the bilayer was found to be 3.28 Å. The lowest energy stacking configuration at a relative orientation of 60° was determined to be AB stacking, and this orientation was used for all the presented calculations. Twenty angstroms of vacuum was used between periodic images normal to the layers. The potentials included the following orbitals in the valence: Mo ($4d^4 5s^2$), W ($5d^4 6s^2$), and Se ($4s^2 4p^4$). The all-electron WIEN2K package was used to confirm the accuracy of the band structure computed with VASP and to compute optical matrix elements.[48]

ASSOCIATED CONTENT

Supporting Information

The Supporting Information is available free of charge on the ACS Publications website at DOI: 10.1021/acsnano.8b01369.

Details of our transfer method, characterization of multiple samples, temperature and power dependence data, and theory details (PDF)

AUTHOR INFORMATION

Corresponding Author

*E-mail: hanbicki@nrl.navy.mil.

ORCID

Aubrey T. Hanbicki: 0000-0001-8200-0378
Matthew R. Rosenberger: 0000-0001-6866-5488
Kathleen M. McCreary: 0000-0003-2737-585X
Berend T. Jonker: 0000-0001-8816-7857

Author Contributions

†A. T. Hanbicki and H.-J. Chuang contributed equally to this research.

Notes

The authors declare no competing financial interest.

‡Postdoctoral associate at the Naval Research Laboratory through the American Society for Engineering Education.

§Postdoctoral associate at the Naval Research Laboratory through the National Research Council.

ACKNOWLEDGMENTS

This research was performed while H.-J.C. held an American Society for Engineering Education fellowship and M.R.R. and S.V.S. held a National Research Council fellowship at NRL. This work was supported by core programs at NRL and the NRL Nanoscience Institute and by the Air Force Office of Scientific Research under contract number AOARD 14IOA018-134141. This work was also supported in part by a grant of computer time from the DoD High Performance Computing Modernization Program at the U.S. Army Research Laboratory Supercomputing Resource Center.

REFERENCES

(1) Mak, K. F.; Lee, C.; Hone, J.; Shan, J.; Heinz, T. F. Atomically Thin MoS_2: A New Direct-Gap Semiconductor. *Phys. Rev. Lett.* **2010**, *105*, 136805.

(2) Splendiani, A.; Sun, L.; Zhang, Y.; Li, T.; Kim, J.; Chim, C.-Y.; Galli, G.; Wang, F. Emerging Photoluminescence in Monolayer MoS_2. *Nano Lett.* **2010**, *10*, 1271−1275.

(3) Geim, A. K.; Grigorieva, I. V. Van Der Waals Heterostructures. *Nature* **2013**, *499*, 419−425.

(4) Akinwande, D.; Petrone, N.; Hone, J. Two-Dimensional Flexible Nanoelectronics. *Nat. Commun.* **2014**, *5*, 5678.

(5) Fang, H.; Battaglia, C.; Carraro, C.; Nemsak, S.; Ozdol, B.; Kang, J. S.; Bechtel, H. A.; Desai, S. B.; Kronast, F.; Unal, A. A.; Conti, G.; Conlon, C.; Palsson, G. K.; Martin, M. C.; Minor, A. M.; Fadley, C. S.; Yablonovitch, E.; Javey, A. Strong Interlayer Coupling in van Der Waals Heterostructures Built from Single-Layer Chalcogenides. *Proc. Natl. Acad. Sci. U. S. A.* **2014**, *111*, 6198−6202.

(6) Tongay, S.; Fan, W.; Kang, J.; Park, J.; Koldemir, U.; Suh, J.; Narang, D. S.; Liu, K.; Ji, J.; Li, J.; Sinclair, R.; Wu, J. Tuning Interlayer Coupling in Large-Area Heterostructures with CVD-Grown MoS_2 and WS_2 Monolayers. *Nano Lett.* **2014**, *14*, 3185−3190.

(7) Gong, Y.; Lin, J.; Wang, X.; Shi, G.; Lei, S.; Lin, Z.; Zou, X.; Ye, G.; Vajtai, R.; Yakobson, B. I.; Terrones, H.; Terrones, M.; Tay, B. K.; Lou, J.; Pantelides, S. T.; Liu, Z.; Zhou, W.; Ajayan, P. M. Vertical and In-Plane Heterostructures from WS_2/MoS_2 Monolayers. *Nat. Mater.* **2014**, *13*, 1135−1142.

(8) Rivera, P.; Schaibley, J. R.; Jones, A. M.; Ross, J. S.; Wu, S.; Aivazian, G.; Klement, P.; Seyler, K.; Clark, G.; Ghimire, N. J.; Yan, J.; Mandrus, D. G.; Yao, W.; Xu, X. Observation of Long-Lived Interlayer Excitons in Monolayer $MoSe_2$−WSe_2 Heterostructures. *Nat. Commun.* **2015**, *6*, 6242.

(9) Rivera, P.; Seyler, K. L.; Yu, H.; Schaibley, J. R.; Yan, J.; Mandrus, D. G.; Yao, W.; Xu, X. Valley-Polarized Exciton Dynamics in a 2D Semiconductor Heterostructure. *Science* **2016**, *351*, 688−691.

(10) Wilson, N. R.; Nguyen, P. V.; Seyler, K.; Rivera, P.; Marsden, A. J.; Laker, Z. P. L.; Constantinescu, G. C.; Kandyba, V.; Barinov, A.; Hine, N. D. M.; Xu, X.; Cobden, D. H. Determination of Band Offsets, Hybridization, and Exciton Binding in 2D Semiconductor Heterostructures. *Sci. Adv.* **2017**, *3*, e1601832.

(11) Nayak, P. K.; Horbatenko, Y.; Ahn, S.; Kim, G.; Lee, J.-U.; Ma, K. Y.; Jang, A.-R.; Lim, H.; Kim, D.; Ryu, S.; Cheong, H.; Park, N.; Shin, H. S. Probing Evolution of Twist-Angle-Dependent Interlayer Excitons in $MoSe_2/WSe_2$ van Der Waals Heterostructures. *ACS Nano* **2017**, *11*, 4041−4050.

(12) Nagler, P.; Plechinger, G.; Ballottin, M. V.; Mitioglu, A.; Meier, S.; Paradiso, N.; Strunk, C.; Chernikov, A.; Christianen, P. C. M.; Schüller, C.; Korn, T. Interlayer Exciton Dynamics in a Dichalcogenide Monolayer Heterostructure. *2D Mater.* **2017**, *4*, 025112.

(13) Miller, B.; Steinhoff, A.; Pano, B.; Klein, J.; Jahnke, F.; Holleitner, A.; Wurstbauer, U. Long-Lived Direct and Indirect Interlayer Excitons in van Der Waals Heterostructures. *Nano Lett.* **2017**, *17*, 5229−5237.

(14) Baranowski, M.; Surrente, A.; Klopotowski, L.; Urban, J. M.; Zhang, N.; Maude, D. K.; Wiwatowski, K.; Mackowski, S.; Kung, Y. C.; Dumcenco, D.; Kis, A.; Plochocka, P. Probing the Interlayer Exciton

DOI: 10.1021/acsnano.8b01369
ACS Nano 2018, 12, 4719−4726

Physics in a $MoS_2/MoSe_2/MoS_2$ van Der Waals Heterostructure. *Nano Lett.* **2017**, *17*, 6360−6365.
(15) Gong, C.; Zhang, H.; Wang, W.; Colombo, L.; Wallace, R. M.; Cho, K. Band Alignment of Two-Dimensional Transition Metal Dichalcogenides: Application in Tunnel Field Effect Transistors. *Appl. Phys. Lett.* **2013**, *103*, 053513.
(16) Kang, J.; Tongay, S.; Zhou, J.; Li, J.; Wu, J. Band Offsets and Heterostructures of Two-Dimensional Semiconductors. *Appl. Phys. Lett.* **2013**, *102*, 012111.
(17) Liang, Y.; Huang, S.; Soklaski, R.; Yang, L. Quasiparticle Band-Edge Energy and Band Offsets of Monolayer of Molybdenum and Tungsten Chalcogenides. *Appl. Phys. Lett.* **2013**, *103*, 042106.
(18) Özçelik, V. O.; Azadani, J. G.; Yang, C.; Koester, S. J.; Low, T. Band Alignment of Two-Dimensional Semiconductors for Designing Heterostructures with Momentum Space Matching. *Phys. Rev. B: Condens. Matter Mater. Phys.* **2016**, *94*, 035125.
(19) Tongay, S.; Zhou, J.; Ataca, C.; Lo, K.; Matthews, T. S.; Li, J.; Grossman, J. C.; Wu, J. Thermally Driven Crossover from Indirect toward Direct Bandgap in 2D Semiconductors: $MoSe_2$ *versus* MoS_2. *Nano Lett.* **2012**, *12*, 5576−5580.
(20) Zeng, H.; Liu, G.-B.; Dai, J.; Yan, Y.; Zhu, B.; He, R.; Xie, L.; Xu, S.; Chen, X.; Yao, W.; Cui, X. Optical Signature of Symmetry Variations and Spin-Valley Coupling in Atomically Thin Tungsten Dichalcogenides. *Sci. Rep.* **2013**, *3*, 1608.
(21) Liu, G.-B.; Shan, W.-Y.; Yao, Y.; Yao, W.; Xiao, D. Three-Band Tight-Binding Model for Monolayers of Group-VIB Transition Metal Dichalcogenides. *Phys. Rev. B: Condens. Matter Mater. Phys.* **2013**, *88*, 085433.
(22) Cadiz, F.; Courtade, E.; Robert, C.; Wang, G.; Shen, Y.; Cai, H.; Taniguchi, T.; Watanabe, K.; Carrere, H.; Lagarde, D.; Manca, M.; Amand, T.; Renucci, P.; Tongay, S.; Marie, X.; Urbaszek, B. Excitonic Linewidth Approaching the Homogeneous Limit in MoS_2 -Based van Der Waals Heterostructures. *Phys. Rev. X* **2017**, *7*, 021026.
(23) Wierzbowski, J.; Klein, J.; Sigger, F.; Straubinger, C.; Kremser, M.; Taniguchi, T.; Watanabe, K.; Wurstbauer, U.; Holleitner, A. W.; Kaniber, M.; Müller, K.; Finley, J. J. Direct Exciton Emission from Atomically Thin Transition Metal Dichalcogenide Heterostructures near the Lifetime Limit. *Sci. Rep.* **2017**, *7*, 12383.
(24) Rooney, A. P.; Kozikov, A.; Rudenko, A. N.; Prestat, E.; Hamer, M. J.; Withers, F.; Cao, Y.; Novoselov, K. S.; Katsnelson, M. I.; Gorbachev, R.; Haigh, S. J. Observing Imperfection in Atomic Interfaces for van Der Waals Heterostructures. *Nano Lett.* **2017**, *17*, 5222−5228.
(25) Rosenberger, M. R.; Chuang, H.-J.; McCreary, K. M.; Hanbicki, A. T.; Sivaram, S. V.; Jonker, B. T. Nano-"Squeegee" for the Creation of Clean 2D Material Interfaces. *ACS Appl. Mater. Interfaces* **2018**, *10*, 10379−10387.
(26) Ceballos, F.; Bellus, M. Z.; Chiu, H.-Y.; Zhao, H. Ultrafast Charge Separation and Indirect Exciton Formation in a MoS_2−$MoSe_2$ van Der Waals Heterostructure. *ACS Nano* **2014**, *8*, 12717−12724.
(27) Rigosi, A. F.; Hill, H. M.; Li, Y.; Chernikov, A.; Heinz, T. F. Probing Interlayer Interactions in Transition Metal Dichalcogenide Heterostructures by Optical Spectroscopy: MoS_2/WS_2 and $MoSe_2/WSe_2$. *Nano Lett.* **2015**, *15*, 5033−5038.
(28) Ross, J. S.; Wu, S.; Yu, H.; Ghimire, N. J.; Jones, A. M.; Aivazian, G.; Yan, J.; Mandrus, D. G.; Xiao, D.; Yao, W.; Xu, X. Electrical Control of Neutral and Charged Excitons in a Monolayer Semiconductor. *Nat. Commun.* **2013**, *4*, 1474.
(29) Singh, A.; Moody, G.; Tran, K.; Scott, M. E.; Overbeck, V.; Berghäuser, G.; Schaibley, J.; Seifert, E. J.; Pleskot, D.; Gabor, N. M.; Yan, J.; Mandrus, D. G.; Richter, M.; Malic, E.; Xu, X.; Li, X. Trion Formation Dynamics in Monolayer Transition Metal Dichalcogenides. *Phys. Rev. B: Condens. Matter Mater. Phys.* **2016**, *93*, 041401.
(30) Courtade, E.; Semina, M.; Manca, M.; Glazov, M. M.; Robert, C.; Cadiz, F.; Wang, G.; Taniguchi, T.; Watanabe, K.; Pierre, M.; Escoffier, W.; Ivchenko, E. L.; Renucci, P.; Marie, X.; Amand, T.; Urbaszek, B. Charged Excitons in Monolayer WSe_2: Experiment and Theory. *Phys. Rev. B: Condens. Matter Mater. Phys.* **2017**, *96*, 085302.
(31) Zhang, C.; Chen, Y.; Johnson, A.; Li, M.-Y.; Li, L.-J.; Mende, P. C.; Feenstra, R. M.; Shih, C.-K. Probing Critical Point Energies of Transition Metal Dichalcogenides: Surprising Indirect Gap of Single Layer WSe_2. *Nano Lett.* **2015**, *15*, 6494−6500.
(32) Xiao, D.; Liu, G.-B.; Feng, W.; Xu, X.; Yao, W. Coupled Spin and Valley Physics in Monolayers of MoS_2 and Other Group-VI Dichalcogenides. *Phys. Rev. Lett.* **2012**, *108*, 196802.
(33) Cao, T.; Wang, G.; Han, W.; Ye, H.; Zhu, C.; Shi, J.; Niu, Q.; Tan, P.; Wang, E.; Liu, B.; Feng, J. Valley-Selective Circular Dichroism of Monolayer Molybdenum Disulphide. *Nat. Commun.* **2012**, *3*, 887.
(34) Mak, K. F.; He, K.; Shan, J.; Heinz, T. F. Control of Valley Polarization in Monolayer MoS_2 by Optical Helicity. *Nat. Nanotechnol.* **2012**, *7*, 494−498.
(35) Yao, W.; Xiao, D.; Niu, Q. Valley-Dependent Optoelectronics from Inversion Symmetry Breaking. *Phys. Rev. B: Condens. Matter Mater. Phys.* **2008**, *77*, 235406.
(36) Zhang, X.-X.; Cao, T.; Lu, Z.; Lin, Y.-C.; Zhang, F.; Wang, Y.; Li, Z.; Hone, J. C.; Robinson, J. A.; Smirnov, D.; Louie, S. G.; Heinz, T. F. Magnetic Brightening and Control of Dark Excitons in Monolayer WSe_2. *Nat. Nanotechnol.* **2017**, *12*, 883−889.
(37) Gao, S.; Yang, L.; Spataru, C. D. Interlayer Coupling and Gate-Tunable Excitons in Transition Metal Dichalcogenide Heterostructures. *Nano Lett.* **2017**, *17*, 7809−7813.
(38) Yu, H.; Liu, G.-B.; Tang, J.; Xu, X.; Yao, W. Moiré Excitons: From Programmable Quantum Emitter Arrays to Spin-Orbit−coupled Artificial Lattices. *Sci. Adv.* **2017**, *3*, e1701696.
(39) Wu, F.; Lovorn, T.; MacDonald, A. H. Theory of Optical Absorption by Interlayer Excitons in Transition Metal Dichalcogenide Heterobilayers. *Phys. Rev. B: Condens. Matter Mater. Phys.* **2018**, *97*, 035306.
(40) Chiu, M.-H.; Li, M.-Y.; Zhang, W.; Hsu, W.-T.; Chang, W.-H.; Terrones, M.; Terrones, H.; Li, L.-J. Spectroscopic Signatures for Interlayer Coupling in MoS_2−WSe_2 van der Waals Stacking. *ACS Nano* **2014**, *8*, 9649−9656.
(41) Hanbicki, A. T.; Currie, M.; Kioseoglou, G.; Hellberg, C. S.; Friedman, A. L.; Jonker, B. T. Optical Polarization of Excitons and Trions under Continuous and Pulsed Excitation in Single Layers of WSe_2. *Nanoscale* **2017**, *9*, 17422−17428.
(42) Perdew, J. P.; Burke, K.; Ernzerhof, M. Generalized Gradient Approximation Made Simple. *Phys. Rev. Lett.* **1996**, *77*, 3865−3868.
(43) Grimme, S.; Antony, J.; Ehrlich, S.; Krieg, H. A Consistent and Accurate *Ab Initio* Parametrization of Density Functional Dispersion Correction (DFT-D) for the 94 Elements H-Pu. *J. Chem. Phys.* **2010**, *132*, 154104.
(44) Grimme, S.; Ehrlich, S.; Goerigk, L. Effect of the Damping Function in Dispersion Corrected Density Functional Theory. *J. Comput. Chem.* **2011**, *32*, 1456−1465.
(45) Kresse, G.; Furthmüller, J. Efficient Iterative Schemes for *Ab Initio* Total-Energy Calculations Using a Plane-Wave Basis Set. *Phys. Rev. B: Condens. Matter Mater. Phys.* **1996**, *54*, 11169−11186.
(46) Kresse, G.; Joubert, D. From Ultrasoft Pseudopotentials to the Projector Augmented-Wave Method. *Phys. Rev. B: Condens. Matter Mater. Phys.* **1999**, *59*, 1758−1775.
(47) Blöchl, P. E. Projector Augmented-Wave Method. *Phys. Rev. B: Condens. Matter Mater. Phys.* **1994**, *50*, 17953−17979.
(48) Blaha, P.; Schwarz, K.; Madsen, G. K. H.; Kvasnicka, D.; Luitz, J. *WIEN2k, An Augmented Plane Wave + Local Orbitals Program for Calculating Crystal Properties*; Techn. Universitat Wien: Austria, 2001.

DOI: 10.1021/acsnano.8b01369
ACS Nano 2018, 12, 4719−4726